PAPER

Check for updates

Self-assembled bamboo-like carbon nanotubes based on chiral H$_8$BINOL sensors to recognize cinchonidine efficiently by diastereoisomer complexes†

Fangxiu Li,[a] Yue Sun,[b] Xiaoxia Sun [ID] *[a] and Yu Hu*[b]

Fluorescence recognition for the antimalarial cinchonidine could be achieved efficiently and rapidly through bamboo-like carbon nanotubes based on chiral conjugated H$_8$BINOL derivatives. Herein, it was proved that the chiral fluorescence probe H$_8$BINOL exhibited excellent fluorescence identification ability for cinchonidine. The structure and size of the *S*-**1** (*S*-(3,3′-phenyl)-5,5′6,6′,7′,8,8′-octahydro-[1,1′-dinaphthalene]-2,2′-diol) and *R*-**1** (*R*-(3,3′-phenyl)-5,5′6,6′,7′,8,8′-octahydro-[1,1′-dinaphthalene]-2,2′-diol) were studied by using the DLS, TEM, and SEM spectra, which exhibited a self-assembled bamboo-like carbon nanotube structure. In the CD (circular dichroism) test, cinchonidine was added to a pair of enantiomers of H$_8$BINOL derivatives. The different configurations of H$_8$BINOL derivatives showed significantly different Cotton effects for cinchonidine, indicating that cinchonidine formed diastereoisomer π–π complexes with different configurations of H$_8$BINOL derivatives. From the AFM tests, it was revealed that cinchonidine could effectively quench the fluorescent spot of the probes quickly. The fluorescence titration tests demonstrated that 6.4×10^{-7} mol of cinchonidine could completely quench the fluorescence sensor of *S*-**1** (2×10^{-5} M, 2 mL) through the formation of a 1 : 1 complex. The limit of detection (LOD) of *S*-**1** was calculated to be 6.08×10^{-10}, which indicates that *S*-**1** has a high sensitivity and can be applied effectively to the practice of identifying cinchonidine. Meanwhile, the fluorescence sensor *R*-**1** also exhibited the same sensibility with a low limit of detection (7.60×10^{-10}).

1. Introduction

The structure and application of chiral nanotubes have attracted immense interest, including their chiral structure, precise control of the structure, and many related applications.[1] Self-assembled nanotubes of organic or biomolecular molecules have also been increasingly studied. For this purpose, π-conjugated molecules with a chiral structure have been designed and synthesized by researchers, and subsequently, chiral nanotubes have been fabricated through self-assembly. The π-conjugated nanotubes exhibit several chiral characteristics, such as tunable circular polarization luminescence and supramolecular chirality, which have potential application value in chiral sensing,[2] three-dimensional display technology, and optoelectronic devices.

[a]Jiangxi Key Laboratory of Organic Chemistry, Jiangxi Science and Technology Normal University, Nanchang, 330013, China. E-mail: sunxiaoxia77@126.com

[b]College of Chemistry, Nanchang University, Nanchang, China

Fluorescence recognition has been considered a promising method in analytical chemistry and biotechnology because fluorescent probes have the advantages of simple operation, use of simple and convenient instruments, relatively low cost, good selectivity, rapid response, and a low detection limit. These probes can be widely used in the detection of metal ions, anions, cations, biomolecules, *etc.*[3,4] Among these probes, the high selectivity and sensitivity of small-molecule fluorescent probes are favoured by biological and chemical researchers in the field of intracellular biological imaging.[5,6] However, small-molecule fluorescent probes exhibit certain drawbacks, such as the low solubility of the probes. Therefore, the development and application of these probes is extremely limited. The chirality of biologically active molecules is one of the trending research topics that aims to explore the evolution and mystery of life itself. Circular dichroism (CD) is the ability of chiral nanomaterials to absorb circularly polarized light of either handedness to varying extents. This property is often used to characterize conformation change and the secondary structure of molecules by measuring the differential extinctions of opposite circularly polarized light in the UV spectral region. Circular dichroism (CD) is exhibited by chiral molecules or

structures that display varying rates of absorption for circularly polarized light of arbitrary handedness. These absorptive properties can provide valuable structural information regarding the materials and the chiral molecules.[7,8]

The cinchona alkaloids, including cinchonine, quinidine, cinchonidine, and quinine, were extracted from the cinchona bark nearly two hundred years ago. These alkaloids represent a series of historically significant medicines and a special backbone of catalysts that have been applied to modern asymmetric syntheses.[9,10] In nature, the quinoline-containing cinchona alkaloids originated from monoterpenoid indole alkaloids. Cinchonidine (α-quinidine) was detected in *Artemisia annua* and cinchona as a basic unit of asymmetric synthesis in organic chemistry. The cinchonidine has been widely used for its antitumor properties and has served as a treatment for malaria for the past few decades.[11,12] As an important pharmaceutical intermediate in organic synthesis, cinchonidine plays an important role in the research and development process of chemical and pharmaceutical medicine. The median lethal dose of cinchonidine is 206 mg kg^{-1}. The rapid and sensitive detection of cinchonidine has huge significance in research.

Chiral substances are highly valued for their unique chemical properties, which have a significant impact on living organisms.[3–15] These unique characteristics enable them to be widely applied in pharmaceutical engineering, bioimaging technology, food industry, and other fields.[16–20] For example, BINOL, a compound with a chiral symmetrical center and a rigid conjugate structure, and its derivatives are notable chiral agents that are commonly used in asymmetric synthesis and catalysis.[21,22] The asymmetric catalytic reaction of BINOL is primarily dependent on its naphthalene ring being a different substituent at different positions.[23–25] H$_8$BINOL, as one of the partial hydrogenation derivatives of BINOL, not only enhances the density of space electron clouds, but also retains the conjugated structure, chirality, and rigidity of BINOL. Despite this, few studies have explored the potential of H$_8$BINOL as a chiral fluorescent probe, and the majority of research work on H$_8$BINOL has focused on its use in asymmetric catalysis.[26–32] Despite being widely used in various fields as a catalyst for research on synthesis, the application of H$_8$BINOL as a chiral self-assembly bamboo-like carbon nanotube and fluorescent probe for detecting cinchonidine has not been reported.

The Suzuki coupling reaction was used to synthesize H$_8$BINOL derivatives, 3,3′-(phenyl)-5,5′6,6′,7,7′,8,8′-octahydro-[1,1′-binaphthalene]-2,2′-diol (*S*-**1**, *R*-**1**). The structure and dimensions of *S*-**1** and *R*-**1** were analyzed using characterization techniques such as DLS, TEM, and SEM images. It was observed that the probes effectively identified cinchonidine and had the ability to greatly extinguish fluorescence within the fluorescence emission spectrum due to the fluorescence resonance energy transfer (FRET) interaction between the probe and cinchonidine.[4,33] *R*-**1** and *S*-**1** demonstrated a high sensitivity and could be applied to the practice of identifying cinchonidine. In addition, it was observed that both the chiral bamboo branching carbon nanotubes *S*-**1** and *R*-**1** exhibited excellent recognition responses to cinchonidine through circular dichroism (CD) and fluorescence experiments by the formation of

diastereoisomer π–π complexes in the ratio 1 : 1, which has never been reported. Therefore, the synthesis of chiral H$_8$BINOL derivatives for identifying cinchonidine probes has promising application value.

2. Results and discussion

The structure of compounds *S*-H$_8$BINOL, *S*-**2**, *S*/*R*-**1**, and cinchonidine are depicted below (Scheme 1). The compounds of *S*-**1** and *R*-**1** based on H$_8$BINOL derivatives synthesized using the phenylboronic acid were obtained by the Suzuki reaction. The yields of *S*-**1** and *R*-**1** were observed to be 70% and 66%, respectively. Coupling reactions are widely used in organic synthesis, owing to its characteristics such as the easy elimination of inorganic byproducts, strong substrate suitability, water insensitivity, and functional group tolerance. The specific synthetic routes for all the compounds are described in the ESI.†

2.1. Characterization of materials *S*-1 and *R*-1

As *S*-**1** and *R*-**1** are a pair of *S*/*R* chiral isomers, their structures are identical. To better explore the structures and sizes of *S*-**1** and *R*-**1**, a series of experiments were carried out to characterize them. To confirm the structures and sizes of *S*-**1** and *R*-**1** aggregates, dynamic laser scattering (DLS), transmission electron microscopy (TEM), and scanning electron microscopy (SEM) were used. The solids of compounds *S*-**1** and *R*-**1** were added to absolute ethanol. The dispersion was prepared by sonicating for 60 s for performing the transmission electron microscopy test, as shown in Fig. 1. The TEM images showed that both the H$_8$BINOL derivatives formed bamboo-like carbon nanotubes. The ends of the compounds were mostly bifurcated branches. Most of the nanotubes were in the range of 200–700 nm in diameter.

To better observe the aggregation state of compound self-assembly, the concentrations of *S*-**1** and *R*-**1** were increased in the SEM tests. The bamboo-like carbon nanotube structures of *S*-**1** and *R*-**1** were also observed in the SEM images, which is
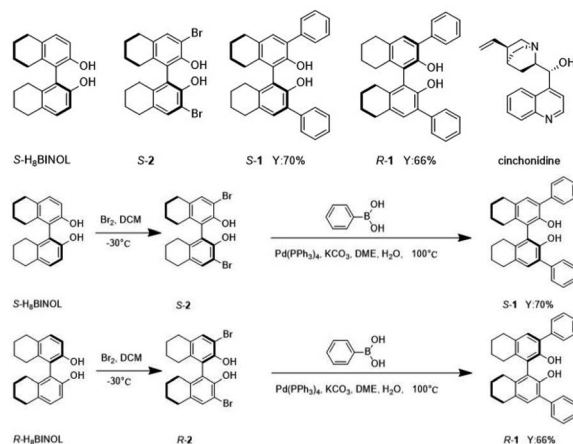
Scheme 1 The structure of compounds *S*-H$_8$BINOL, *S*-**2**, *S*/*R*-**1** and cinchonidine. And the synthetic routes of *S*-**1** and *R*-**1**.
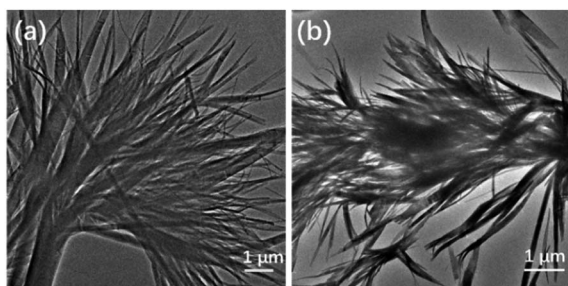
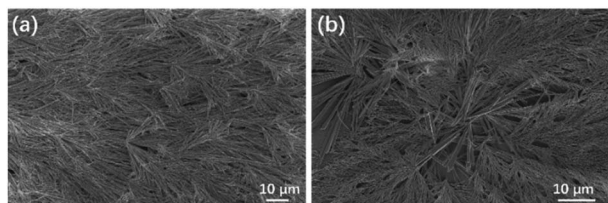**Fig. 1** (a) The TEM image of the *S*-**1**. (b) The TEM image of the *R*-**1**.

Fig. 2 (a) The SEM image of the *S*-**1**. (b) The SEM image of the *R*-**1**.
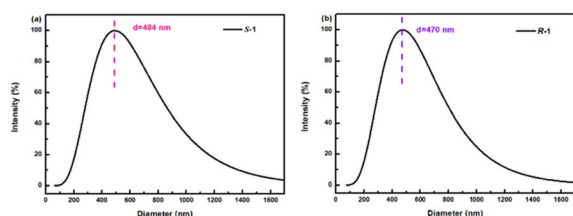

Fig. 3 (a) The DLS of *S*-**1** in ethanol. (b) The DLS of *R*-**1** in ethanol.

consistent with the observations in the TEM images (in Fig. 2a and b). Due to the increased concentration of the compounds in the SEM tests, the force of self-assembly between the molecules was stronger, and the annotation of the medium-shaped carbon nanotubes was also dense. *S*-**1** was detected through DLS in an ethanol dispersion with a diameter ranging from 100–1000 nm, as shown in Fig. 3a.

2.2. The CD spectrum of *S*-**1**, *R*-**1**, *S*-**1** with cinchonidine and *R*-**1** with cinchonidine

To better study the chiral identification ability of the compounds *S*-**1** and *R*-**1**, circular dichroism chromatography (CD) and fluorescent detection experiments were carried out. In Fig. 4a, *S*-**1** and *R*-**1** exhibit obvious opposite Cotton signals in the wavelength range of 200–330 nm, with several peaks at wavelengths 205 nm, 217 nm, 238 nm, 262 nm, 286 nm, and 306 nm. After the addition of cinchonidine, the negative Cotton signals of *S*-**1** at 205 nm and 218 nm were both amplified, whereas the positive Cotton signals of *R*-**1** at 205 nm and 217 nm were also enhanced. This trend certifies the different optical properties of the diastereoisomer complexes formed by the different configurations of the H$_8$BINOL derivatives *S*/*R*-**1** and cinchonidine. The cotton peak at 205 nm is due to a π–π* electronic transition, while the cotton peak at 205 nm is because of
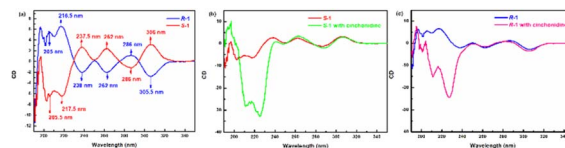

Fig. 4 (a) The CD spectrum of *S*-**1** and *R*-**1**. (b) The CD spectrum showed changes in *S*-**1** and *S*-**1** with cinchonidine. (c) The CD spectrum showed changes in *R*-**1** and *R*-**1** with cinchonidine.

the contribution of an n–π* electronic transition. Moreover, when cinchonidine was added to *S*-**1**, the Cotton signal of *S*-**1** was still negative, indicating that the addition of cinchonidine only changed the microenvironment of *S*-**1** and not its optical rotation, which is regarded as chiral retention. Notably, the positive Cotton signal of *R*-**1** became negative after adding the cinchonidine, implying that the addition of cinchonidine led to the formation of a complex between *R*-**1** and cinchonidine. At the same time, after the addition of cinchonidine, the negative Cotton signals of *S*-**1** at 205 nm and 218 nm and the positive Cotton signals of *R*-**1** at 205 nm and 217 nm were all red-shifted. This trend further demonstrated the π–π interactions between cinchonidine and *S*/*R*-**1**. Fig. 4b and c depicts that the addition of cinchonidine only affected the changes in the CD signal at 200–230 nm, whereas the CD signal after 230 nm hardly exhibited any change.

2.3. Fluorescence testing applications

Firstly, *S*-**1** and *R*-**1** were dissolved in chromatographic methanol with a probe concentration of 2.0×10^{-5} M. Subsequently, seven different chiral splitting agents or chiral asymmetric catalytic species, such as (1*S*,2*S*)-1,2-diphenylethylenediamine, *S*-phenethylamine, ᴅ-2-aminobutyric acid, *S*-2-amino-1-phenylethanol, (1*S*,2*S*)-1,2-cyclohexanediamine, cinchonidine, and ᴅ-tertleucinol, were prepared with a concentration of 0.025 M. When five eq. chiral species were added sequentially to probe *S*-**1**, *S*-**1** demonstrated significant decreases in fluorescence response to cinchonidine at $\lambda_{exc} = 270$ nm. On the other hand, the other chiral reagents did not exhibit a significant fluorescence response, with hardly a shift in the wavelength (in ESI, Fig. S9†). The fluorescence recognition of *R*-**1** was consistent with that of *S*-**1**, indicating that both *S*-**1** and *R*-**1** had evident fluorescence selectivity for cinchonidine. These changes suggest that *S*-**1** and *R*-**1** can selectively identify cinchonidine.

Fig. 5 depicts more detailed fluorescence tests for *S*-**1** *versus* cinchonidine. Fig. 5a is a fluorescence map of *S*-**1** and its recognition of five eq. cinchonidine, which reflects the high sensitivity of the *S*-**1** probe. To demonstrate the changes in fluorescence recognition of *S*-**1** with respect to cinchonidine more effectively, a series of fluorescence titrations were performed. The results are depicted in Fig. 5b. With the continuous release of the ethanol solution of cinchonidine into the test solution of *S*-**1**, the fluorescence intensity of the system continued to decrease. When 16 eq. of the cinchonidine solution was added dropwise to the *S*-**1** test solution, the fluorescence was quenched. This indicates that *S*-**1** has a clear fluorescence response to cinchonidine. As displayed in Fig. 5c, the limit of detection (LOD) of *S*-**1** was calculated to be 6.08 ×
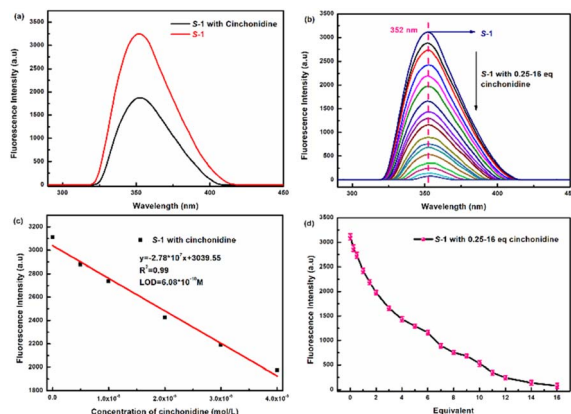
Fig. 5 (a) Fluorescence spectra of S-1 (2.0 × 10⁻⁵ M) toward cinchonidine (5 eq., 0.025 M) (λ_{ex} = 270 nm, slits: 5.0/5.0 nm). (b) Titrated S-1 fluorescence titration with 0.25–16 eq. of cinchonidine. (c) The limit of detection of S-1. (d) Trends of fluorescence changes of S-1 after the addition of 0.25–16 eq. cinchonidine.

Fig. 6 (a) Fluorescence spectra of R-1 (2.0 × 10⁻⁵ M) toward cinchonidine (5 eq., 0.025 M) (λ_{ex} = 270 nm, slits: 5.0/5.0 nm). (b) Titrated R-1 fluorescence titration with 0.25–16 eq. of cinchonidine. (c) The limit of detection of R-1. (d) Comparison of S-1 and R-1 fluorescence trends after adding 0.25–16 eq. cinchonidine.

10^{-10}, which indicates that S-1 exhibits a high sensitivity and can be applied to the practice of identifying cinchonidine. Trends of changes in fluorescence response of S-1 after the addition of 0.25–16 eq. cinchonidine are shown in Fig. 5d. Cinchonidine underwent individual fluorescence and UV tests, and the relevant spectral information are given in ESI.†

To better determine the binding ratio of S-1 and cinchonidine, fluorescence complexation titration experiments with S-1 mixed with cinchonidine were performed. The experimental results are shown in Fig. S10.† When the molar fraction ratio of [cinchonidine]/([cinchonidine] + [S-1]) increased to 0.5, the molar fraction of [S-1] reached a maximum. As the [cinchonidine]/([cinchonidine] + [S-1]) molar fraction ratio continued to increase, the [S-1] molar fraction gradually decreased, indicating that the complex ratio between probe S-1 and the cinchonidine molecule was 1 : 1. Having a binding ratio of 1 : 1 has excellent implications for the analysis of the fluorescence recognition of S-1 with respect to cinchonidine.

More detailed fluorescence tests for R-1 *versus* cinchonidine were performed, and the findings are shown in Fig. 6. As shown in Fig. 6a, when five eq. of the ethanol solution cinchonidine was added to R-1 at λ_{ex} = 270 nm, the fluorescence response of cinchonidine to R-1 was more obvious, fluorescence intensity was weakened, and the wavelength hardly changed. As shown in Fig. 6b, with the continuous release of the ethanol solution of cinchonidine (0.25–16 eq.) to the test solution of R-1, the fluorescence intensity of the system continued to decrease. When 16 eq. of the cinchonidine solution was added dropwise to the R-1 test solution, fluorescence was quenched. This indicates that R-1 exhibits a clear fluorescence response to cinchonidine. As displayed in Fig. 6c, the limit of detection (LOD) of R-1 was calculated to be 7.60×10^{-10}. A comparison of the fluorescence trends of S-1 and R-1 after adding 0.25–16 eq. cinchonidine is shown in Fig. 6d. Overall, the fluorescence recognition trends of S-1 and R-1 for the chiral compound of cinchonidine were consistent. However, the fluorescence selectivity of S-1 for cinchonidine was superior to that of R-1.
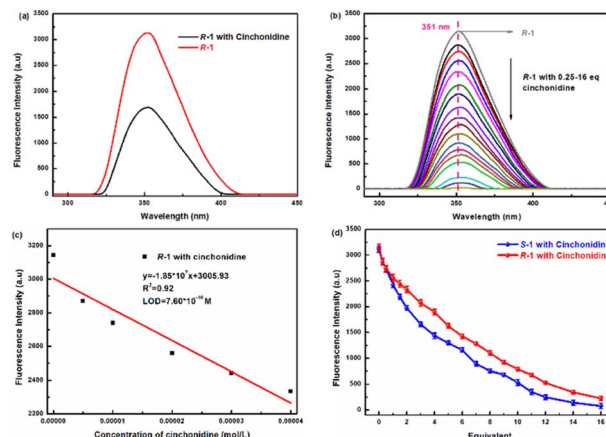
The Benesi–Hildebrand equation was fitted to the plot of $F_0/(F_0 - F)$ *versus* 1/[cinchonidine], and the values of the association constant K_a of R-1 or S-1 with respect to cinchonidine were acquired from the slope. Meanwhile, the K_a value for the R-1–cinchonidine complex was determined to be 2.55×10^4 M⁻¹, while the K_a value for the S-1–cinchonidine complex was determined to be 1.43×10^4 M⁻¹. Previous studies have shown that complexation constants of moderate binding appear within the range of 10^2 to 10^4 M⁻¹. Therefore, it could be verified that the binding between both enantiomers and cinchonidine was medium. The complex constant of R-1 is greater than that of S-1, which indicates that R-1 is more easily combined with cinchonidine to form diastereoisomers. The plot of $F_0/(F_0 - F)$ *versus* 1/[cinchonidine] for (a) S-1 (b) R-1 is shown in Fig. S12.†

2.4. The recognition application of cinchonidine by the sensor through the AFM tests

For the rapid and effortless detection of cinchonidine by the sensors S-1 and R-1, atomic force microscopy tests (AFM) were applied to detect cinchonidine. From the AFM tests, the ethanol dispersion solutions of S-1 and R-1 were released dropwise to the slide, both exhibiting bright yellow fluorescent spots, as shown in Fig. 7a and c. This indicates the fluorescent signature of the molecules. Subsequently, we continued to add six eq. of the cinchonidine solution dropwise to the ethanol solution of S-1 and R-1, and the fluorescence spots in the final AFM image became much weaker than before (in Fig. 7b and d) at a rapid rate. By comparing the images obtained before and after releasing cinchonidine, it can be concluded that cinchonidine can effectively quench the fluorescence of S-1 and R-1.

2.5. The mechanism of recognition

2.5.1 X-ray crystallographic analyses of R-1. In order to study the mechanism of molecular recognition, the single crystal structure of the compound R-1 was studied first. The three-dimensional structure and spatial distribution of the
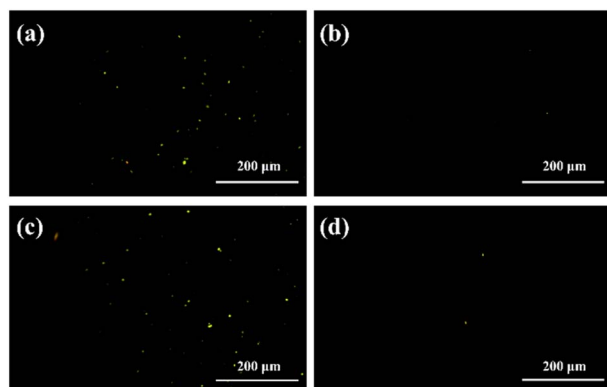
Fig. 7 (a) The AFM image of the *S*-**1**. (b) The AFM image of the *S*-**1** with 6 eq. cinchonidine. (c) The AFM image of the *R*-**1**. (d) The AFM image of the *R*-**1** with 6 eq. cinchonidine.

compound *R*-**1** were further demonstrated through X-ray tests. Single crystal X-ray analysis showed that the *R*-**1** molecules were arranged neatly and had the same structure in each cell, while the molecules self-assembled into an ordered structure in Fig. 8a and b. The dihedral angle of the *R*-**1** was 86.49°, indicating that the chiral planes of the biphenyl axis in the *R*-**1** molecules were basically vertical. The vertical distance of the phenyl group at position 3 of the two adjacent *R*-**1** molecules was 4.808 A, which indicated that a certain π–π force existed between the molecules. A π–π stacking structure existed when the *R*-**1** molecule was assembled as a supramolecular system, as shown in Fig. 8d. The analysis of the results of the single crystal of *R*-**1** is of immense significance for the study of the recognition mechanism of cinchonidine.

2.5.2 The ^{1}HNMR titration of *S*-1 and cinchonidine. To further understand the mechanism of the fluorescent responses of the probe *S*-**1** (1.0×10^{-5} M) for cinchonidine, we performed ^{1}HNMR titration experiments. Fig. S13† shows the ^{1}HNMR spectra when *S*-**1** (1.0×10^{-5} M in deuterated DMSO) was treated with cinchonidine in different equivalents.

As observed in the ^{1}HNMR titration diagram of Fig. S13,† cinchonidine had a phenolic hydroxyl hydrogen signal (Ha) in the solvent of deuterated DMSO at δ 5.71. Upon the continuous

addition of cinchonidine to *S*-**1**, additional hydrogen signals in cinchonidine emerged gradually, while the signal of Ha disappeared at 5.64 ppm. This trend indicates the formation of a complex between *S*-**1** and cinchonidine. Since no obvious signal changes were observed, it may be due to a weak intermolecular interaction force between the *S*-**1** and cinchonidine. By analyzing the benzene ring structure of the cinchonidine identified by *S*-**1**, it could be assumed that this force is a π–π stacking interaction. Further investigation into the binding mechanisms between *S*-**1** and cinchonidine is ongoing.

2.5.3 The mechanism of the responses of *R*/*S*-1 toward cinchonidine. As exhibited in Fig. S15,† the cinchonidine served as a fluorophore. The fluorescence quenching mechanism of the self-assembled nanomaterial *R*-**1** may be attributed to the fluorescence resonance energy transfer (FRET) and inner filter effect (IFE). In order to study the fluorescence quenching mechanism of cinchonidine recognized by *R*-**1**, the excitation and emission spectra of the sensor solution and the UV-VIS absorption spectra of cinchonidine were measured. The ultraviolet and fluorescence test results showed that there was a significant overlap between the UV adsorption of cinchonidine and the excitation spectrum of *R*-**1**, as shown in Fig. 9a. The absorption of cinchonidine at 270 nm could effectively inhibit the excitation energy absorption of *R*-**1**. The addition of cinchonidine significantly quenched the fluorescence of *R*-**1**, which may be attributed to the IFE or FRET mechanism. The fluorescence lifetime of fluorophore evidently varies in the FRET mechanism, but hardly changes in the IFE. Consequently, the fluorescence lifetime of *R*-**1** and *R*-**1**–cinchonidine were measured to further analyze the fluorescence quenching mechanism of *R*-**1**. As shown in Fig. 9b, the calculated average fluorescence lifetime of *R*-**1** is 1.12 ns. After adding
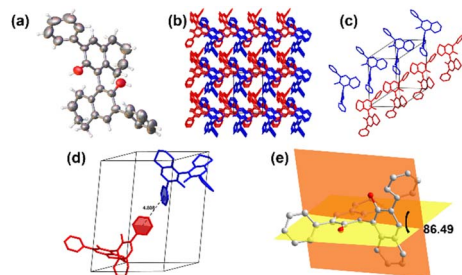

Fig. 8 (a) The spatial structure of *R*-**1**. (b) The pi–π packing diagram of *R*-**1** molecules. (c) Stacking diagram between adjacent *R*-**1** molecules. (d) The vertical distance between the 3-position benzene rings of the *R*-**1** molecules. (e) The angle between two naphthalene ring planes in the *R*-**1** molecule.
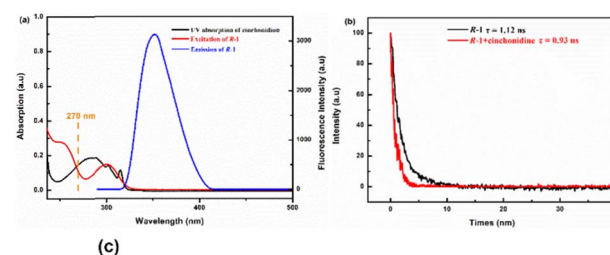
Fig. 9 (a) The UV absorption spectrum of cinchonidine and excitation and emission spectra of *R*-**1**. (b) The fluorescence lifetime decay curve of *R*-**1** in the presence and absence of cinchonidine. (c) The propose mechanism of the responses of *R*/*S*-**1** toward cinchonidine.
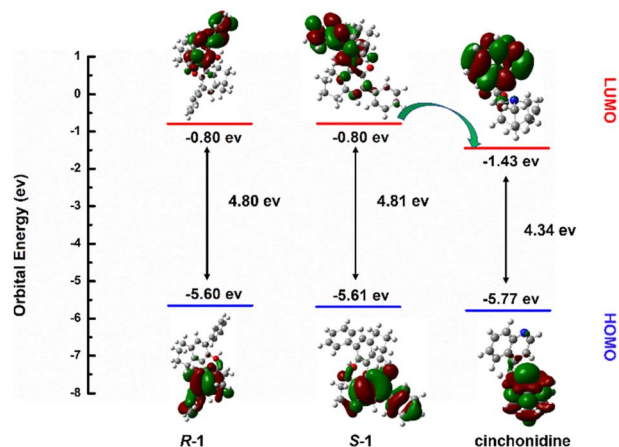
Fig. 10 DFT calculation of *R*-**1**, *S*-**1** cinchonidine.

cinchonidine, the mean fluorescence lifetime of *R*-**1** became 0.93 ns, which was inconsistent with the results obtained previously from *R*-**1**. These results confirm the presence of FRET in the quenching mechanism of cinchonidine that was recognized by *R*-**1** as shown in Fig. 9c. In the FRET, the benzene ring at the outer end of *R*-**1** served as an electron donor, and the N of cinchonidine served as an electron acceptor. This implies that the energy can be transferred from *R*-**1** to cinchonidine.

2.5.4 DFT calculation. In order to further verify the electron distribution between *R*/*S*-**1** and cinchonidine, the density functional theory (DFT) at B3LYP/6-31G (d) was used to calculate.[34] The electron cloud density distributions of the highest occupied orbit (HOMO) and lowest unoccupied orbit (LUMO) of *R*/*S*-**1** and cinchonidine are shown in Fig. 10. The difference in the values of E_g of *R*/*S*-**1** was 0.01 eV, which indicates that the chiral structure of *R*/*S*-**1** had little effect on the energy level. The LUMO orbitals could accept electrons, and the lower the energy, the more favorable it is for electron filling. The results of the DFT showed that the LUMO orbital energy of cinchonidine was significantly lower than that of *R*/*S*-**1**. This indicates that the 3-position phenyl group of *R*/*S*-**1** can transfer electrons to the N of cinchonidine, thus realizing the intermolecular FRET mechanism.

3. Experimental section

3.1. Materials

The experimental reagents were purchased from Innochem in Beijing, and all chemicals were purchased from Aladdin. In addition, dichloromethane, ethanol, and methanol were ultra-dry solvents.

3.2. Instrumentation

The Atomic Force Microscopy (AFM) images were measured using OLYMPUS DP74. Fluorescence spectrum experiments were conducted on an FL-970Plus fluorescence spectrophotometer. The FEI Tecnai F20 (Thermo, America) Transmission Electron Microscope (TEM) was used to take TEM images. The Rudolf AUTOPOL IV automatic polarimeter measured optical rotation data. DLS data were measured using Brookhaven NanoBrook 90 Plus. The single crystal X-ray was acquired on Smart Apex II. A Bruker AM-400WB spectrometer measured NMR. The SEM images of *S*-**1** and *R*-**1** were acquired on Philips-FEI Tecnai G2S-Twin microscope. Circular dichroism (CD) spectroscopy data were measured using JASCO810. Melting point tests of *S*-**1** and *R*-**1** used the X-4 melting point tester.

3.3. Preparation of material

The synthesis steps of *S*/*R*-**1** and *S*/*R*-**2** and the ^{1}H NMR and {^{1}H}^{13}C NMR of all compounds are described in detail in the ESI.†

3.4. Theoretical calculations

The quantum chemical calculations were performed using the DFT method within the Gaussian 09 package. The equilibrium geometries were calculated through the hybrid exchange-correlation function Becke three parameters hybrid exchange-correlation functional (B3LYP). During structure optimization, the basis set of 6-31 G(d) was chosen for the other light atoms, *i.e.*, the C, H, O, and N atoms. The solvation effects were considered by the polarizable continuum model (PCM), which simulated the solvation effect in the aqueous solution. The hydrogen-bond interaction was calculated using the dispersion correction (gd3bj).

4. Conclusions

In summary, phenyl fluorescent probes *S*-**1** and *R*-**1** were designed and synthesized by using the Suzuki coupling reactions based on the chiral characteristics of H_8BINOL. Firstly, material characterization of *S*-**1** and *R*-**1** were performed through transmission electron microscopy (TEM), scanning electron microscopy (SEM), and atomic force microscopy (AFM). In the TEM images, both the *S*-**1** and *R*-**1** molecules exhibited dendritic carbon nanotube structures, which are hollow structures. The SEM images further demonstrated the appearance and topography of the dendritic structures of the material molecules in detail. In the SEM and TEM images, the diameter ranges of the carbon nanotubes of *S*-**1** and *R*-**1** were shown to be 200–700 nm. The chiral distinction between *S*-**1** and *R*-**1** was assessed by using circular dichroic chromatography, and it was shown that the CD signal was highly symmetrical in the wavelength range of 200–300 nm.

According to the fluorescence tests, adding 6.48×10^{-7} mol cinchonidine to the probe could completely quench probe fluorescence through the formation of 1 : 1 complex. The limit of detection (LOD) of *S*-**1** was calculated to be 6.08×10^{-10}, while the limit of detection (LOD) of *R*-**1** was calculated to be 7.60×10^{-10}, which indicated that both enantiomers had a high sensitivity and can be applied to the practice of identifying cinchonidine. After the addition of cinchonidine to *S*-**1** and *R*-**1**, the signal intensity of the CD signal at a wavelength range of 210–230 nm was significantly changed. The different cotton reactions indicated that cinchonidine and *R*-**1**/*S*-**1** formed diastereoisomer complexes. The negative Cotton signals of *S*-**1** at

205 nm and 218 nm and the positive Cotton signals of *R*-**1** at 205 nm and 217 nm were all red-shifted, which further demonstrated the π–π interactions between cinchonidine and *S*/*R*-**1**. From the AFM tests, it was observed that the ethanol dispersion solutions of *S*-**1** and *R*-**1** exhibited bright yellow fluorescent spots. When cinchonidine was added, the bright yellow fluorescent dots of sensors *S*-**1** and *R*-**1** rapidly disappeared. Cinchonidine could be quickly and easily detected through AFM observation.

As an important intermediate in organic synthesis, cinchonidine plays an important role in the research and development process of chemical and pharmaceutical medicine. Herein, the obtained *S*-**1** and *R*-**1** probes showed a highly stability, a robust framework, and could be successfully applied to the fluorescence recognition of cinchonidine, which can have important application value.

Author contributions

Fangxiu Li and Yue Sun carried out the experiments, analyzed and interpreted the data, and wrote the manuscript. Xiaoxia Sun and Yu Hu took the leadership responsibility for the research activity planning. All authors have read and agreed to the published version of the manuscript.

Conflicts of interest

There are no conflicts to declare.

Notes and references

1 K. Takaishi, K. Iwachido and T. Ema, *J. Am. Chem. Soc.*, 2020, **142**, 1774–1779.

2 F. Yang, M. Wang, D. Zhang, J. Yang, M. Zheng and Y. Li, *Chem. Rev.*, 2020, **120**, 2693–2758.

3 X. Liang, X. Xu, D. Qiao, Z. Yin and L. Shang, *Chem.–Asian J.*, 2017, **12**, 3187–3194.

4 V. V. Koppal, P. G. Patil, R. M. Melavanki, R. A. Kusanur, U. O. Afi and N. R. Patil, *J. Mol. Liq.*, 2019, **292**, 111419.

5 P. Xie, F. Guo, L. Wang, S. Yang, D. Yao and G. Yang, *J. Fluoresc.*, 2015, **25**, 319–325.

6 H. Fang, Y. Chen, Z. Jiang, W. He and Z. Guo, *Acc. Chem. Res.*, 2023, **56**, 258–269.

7 P. Spaeth, S. Adhikari, M. D. Baaske, S. Pud, J. Ton and M. Orrit, *ACS Nano*, 2021, **15**, 16277–16285.

8 X. Sun, J. Yang, L. Sun, G. Yang, C. Liu, Y. Tao, Q. Cheng, C. Wang, H. Xu and Q. Zhang, *ACS Nano*, 2022, **16**, 19174–19186.

9 W. Liu, W. Qin, X. Wang, F. Xue, X.-Y. Liu and Y. Qin, *Angew. Chem., Int. Ed.*, 2018, **57**, 12299–12302.

10 A. Akdeniz, L. Mosca, T. Minami and P. Anzenbacher, *Chem. Commun.*, 2015, **51**, 5770–5773.

11 D. Tang, X. Wang, J. Wu, Y. Li, C. Li, X. Qiao, L. Fan, Y. Chen, H. Zhu, Z. Zhang and Y. He, *CNS Neurosci. Ther.*, 2023, 1–12.

12 Q.-M. Xu, D. Wang, L.-J. Wan, C.-L. Bai and Y. Wang, *J. Am. Chem. Soc.*, 2002, **124**, 14300–14301.

13 Y. Zhao, X. Zhu, W. Jiang, H. Liu and B. Sun, *Molecules*, 2021, **26**, 1145.

14 T. Liu, Z. Li, J. Wang, J. Chen, M. Guan and H. Qiu, *Chem. Eng. J.*, 2021, **410**, 128247.

15 R. Chen, X. Qiao and F. Liu, *Anal. Chim. Acta*, 2022, **1201**, 339632.

16 I. Boussouar, Q. Chen, X. Chen, Y. Zhang, F. Zhang, D. Tian, H. S. White and H. Li, *Anal. Chem.*, 2017, **89**, 1110–1116.

17 S. Zhang, X. Chen, L. Sun and H. Li, *ACS Appl. Nano Mater.*, 2020, **3**, 4351–4356.

18 B. Kasprzyk-Hordern and D. R. Baker, *Environ. Sci. Technol.*, 2012, **46**, 1681–1691.

19 A. Qu, L. Xu, C. Xu and H. Kuang, *Chem. Commun.*, 2022, **58**, 12782–12802.

20 Y.-P. He, L.-B. Yuan, J.-S. Song, G.-H. Chen, Q. Lin, C. Li, L. Zhang and J. Zhang, *Chem. Mater.*, 2018, **30**, 7769–7775.

21 M. J. Baruah, T. J. Bora, G. Gogoi, N. Hoque, N. K. Gour, S. K. Bhargava, A. K. Guha, J. K. Nath, B. Das and K. K. Bania, *J. Colloid Interface Sci.*, 2022, **608**, 1526–1542.

22 B. A. Jones, T. Balan, J. D. Jolliffe, C. D. Campbell and M. D. Smith, *Angew. Chem., Int. Ed.*, 2019, **58**, 4596–4600.

23 R. Peng, L. Lin, X. Wu, X. Liu and X. Feng, *J. Org. Chem.*, 2013, **78**, 11602–11605.

24 T. Song, Y. Cao, G. Zhao and L. Pu, *Inorg. Chem.*, 2017, **56**, 4395–4399.

25 L. Pu, *Acc. Chem. Res.*, 2017, **50**, 1032–1040.

26 A. M. DeBerardinis, M. Turlington, J. Ko, L. Sole and L. Pu, *J. Org. Chem.*, 2010, **75**, 2836–2850.

27 Y. Yue, M. Turlington, X.-Q. Yu and L. Pu, *J. Org. Chem.*, 2009, **74**, 8681–8689.

28 J. Ying, X.-D. Wu, D. Wang and L. Pu, *J. Org. Chem.*, 2016, **81**, 8900–8905.

29 S. Yu, A. M. DeBerardinis, M. Turlington and L. Pu, *J. Org. Chem.*, 2011, **76**, 2814–2819.

30 R. Kshatriya, *ACS Omega*, 2023, **8**, 17381–17406.

31 C. Wang, P. Anbaei and L. Pu, *Chem.–Eur. J.*, 2016, **22**, 7255–7261.

32 R. Bellini and J. N. H. Reek, *Chem.–Eur. J.*, 2012, **18**, 7091–7099.

33 L. Xiao, X. Xiaoyi, Q. Dan, Y. Zheng and S. Luqing, *Chem.–Asian J.*, 2017, **12**, 3187–3194.

34 H. Feng, J. Pu, S. Wang, S. Jiang, W. Yang, D. Cao and Y. Feng, *Dyes Pigm.*, 2023, **217**, 111422.